ACS APPLIED MATERIALS & INTERFACES

www.acsami.org

Research Article

Understanding Process–Structure Relationships during Lamination of Halide Perovskite Interfaces

Clare L. Lanaghan,[†] Oluka Okia,[†] Thomas Coons, Srinivas K. Yadavalli, Jack R. Palmer, Mengyao Zhang, Karrer Hersh, Moses Kodur, Orlando Trejo, Sean P. Dunfield, M. D. Thouless, David P. Fenning, Xun Huan, and Neil P. Dasgupta*

Cite This: *ACS Appl. Mater. Interfaces* 2024, 16, 58657–58667

Read Online

ACCESS | Metrics & More | Article Recommendations | Supporting Information

ABSTRACT: Fabrication of halide perovskite (HP) solar cells typically involves the sequential deposition of multiple layers to create a device stack, which is limited by the thermal and chemical incompatibility of top contact layers with the underlying HP semiconductor. One emerging strategy to overcome these restrictions on material selection and processing conditions is lamination, where two half-stacks are independently processed and then diffusion bonded to complete the device. Lamination reduces the processing constraints on the top side of the solar cell to allow new device designs, expanded use of deposition methods, and self-encapsulation of devices. While laminated perovskite solar cells with high efficiencies and novel interlayer combinations have been demonstrated, there is a limited understanding of how the lamination process parameters affect the diffusion-bond quality and material properties of the resulting HP layer. In this study, we systematically vary temperature, pressure, and time during lamination and quantify the resulting impacts on bonded area, grain domain size, and photoluminescence. A design of experiments is performed, and statistical analysis of the experimental results is used to quantitatively evaluate the resulting process–structure–property relationships. The lamination temperature is found to be the key parameter controlling these properties. A temperature of 150 °C enables successful bonding over 95% of the substrate area and also results in increases in apparent grain domain size and photoluminescence intensity. Based on these insights, the lamination temperature of functional perovskite solar cell devices is varied, demonstrating the importance of the resulting bond quality on device performance metrics.

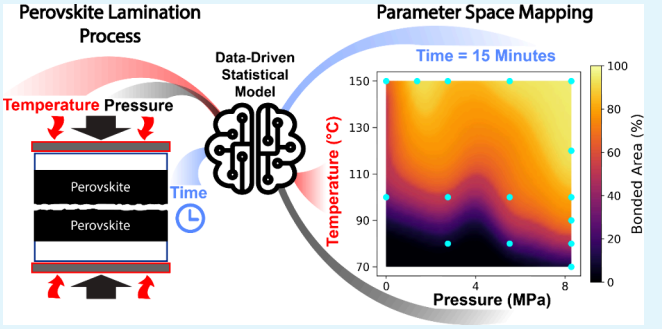

KEYWORDS: *perovskite, solar cells, lamination, Gaussian process modeling, manufacturing*

INTRODUCTION

Perovskite solar cells (PSCs) have emerged as a promising technology for efficient and cost-effective photovoltaic energy conversion. Halide perovskites (HPs) offer several advantageous properties, including high efficiencies, the use of earth-abundant materials, and the potential for low-cost, scalable production. However, several challenges hinder their widespread adoption, including limitations in their stability and manufacturability.[1−4]

Perovskite solar cells are commonly fabricated through a sequential layer-by-layer deposition process, in which each layer of the solar cell (transport, passivation, contact layers, HP film) is fabricated on top of the preceding layer. However, during sequential deposition, the processing of the top transport, passivation, and contact layers (whether using a p-i-n or n-i-p structure) are restricted by the chemical and thermal constraints of the underlying HP layer. Lamination is an emerging processing strategy that can overcome the challenges of sequential deposition, enabling new PSC device designs that are not possible using sequential-deposition methods. For example, this approach was shown to enable devices with dual-passivation of both the electron transport layer (ETL)/HP and hole transport layer (HTL)/HP interfaces using self-assembled monolayers (SAMs), which would be difficult to achieve using sequential deposition processes.[5]

An example of lamination processing involves the integration of two independently processed half-stacks, which are each comprised of an electrical contact, transport layer, and perovskite layer (Scheme 1). The two half-stacks are bonded to form a complete laminated perovskite solar cell (L-PSC). In this approach, the transport, passivation, and contact layers on

Received: July 24, 2024
Revised: September 30, 2024
Accepted: October 2, 2024
Published: October 15, 2024

https://doi.org/10.1021/acsami.4c12379
ACS Appl. Mater. Interfaces 2024, 16, 58657–58667

Scheme 1. Lamination Process Flow[a]

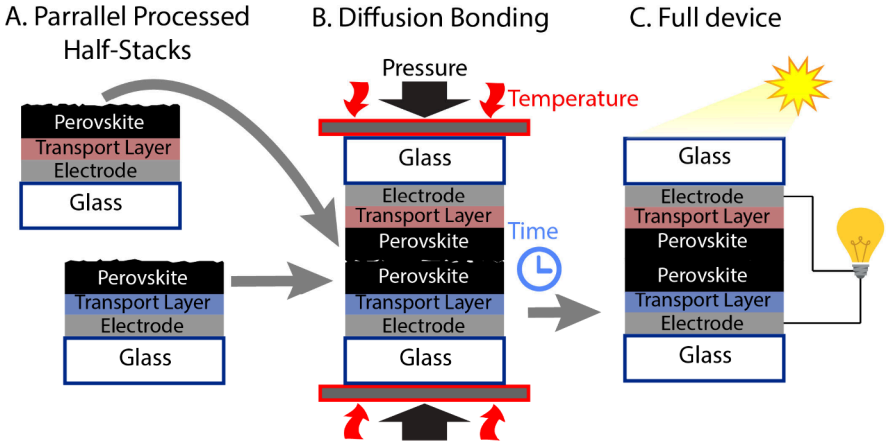

[a](A) Parallel fabrication of separate half-stacks, with the HP material as the final (top) layer. (B) Lamination of the two half-stacks through the application of elevated temperature and pressure. (C) Resulting L-PSC device architecture.

both sides of the cell are processed prior to depositing the HP film.[4−10] Lamination thus allows for the use of deposition processes such as solution processing with incompatible solvents, vapor deposition using reactive precursors, and/or high temperature annealing, which cannot be performed on top of the HP film in the device stack.[5,9]

Furthermore, L-PSCs can utilize glass substrates on both sides of the device, which facilitates self-encapsulation to improve device stability.[6,11] This self-encapsulation enables thermal processing of the HP film at elevated temperatures that would otherwise degrade the HP material.[7,8,12] For example, we have previously shown that conventional annealing of the $FA_{0.8}MA_{0.15}Cs_{0.05}PbI_{2.6}Br_{0.4}$ perovskite material used in this study at 150 °C results in an increase in the presence of the PbI_2 phase in the film relative to the HP phase, while lamination between two glass substrates at the same temperature resulted in a decrease in the ratio of the PbI_2 phase relative to the HP phase.[5] This is attributed to the "confined annealing" condition during lamination, where the self-encapsulation between two glass substrates minimizes the likelihood of outgassing of the volatile organic cation species from the film.

Various combinations of transport layers and lamination interfaces have been used to create L-PSCs in recent years. These have resulted in devices with an increased efficiency and improved stability. The initial study in 2018 reported diffusion bonding at a perovskite-perovskite interface with a cell efficiency of 10%.[7] Since then, functional devices have been laminated at the perovskite-perovskite and perovskite-transport layer interfaces, achieving efficiencies up to 22.3%.[13] As an alternative strategy, conductive glue layers have also been used as an interfacial adhesive to promote lamination.[6,8−10]

While lamination represents a promising manufacturing strategy for PSCs, most studies to date have focused on device fabrication and characterization, with limited knowledge on the detailed process-structure relationships that occur during diffusion bonding at the perovskite-perovskite interface. As illustrated in Scheme 1, diffusion bonding at this interface is of particular interest for lamination because of the high ionic diffusivity of HP materials, as well as the ability to separately form, passivate, and optimize the HP/transport layer interfaces prior to the final lamination step.

The application of elevated temperatures and pressures is known to result in changes in both the microstructure and phase purity of HP films. For example, unencapsulated perovskite films have been shown to degrade and form PbI_2 at elevated temperatures above 110 °C.[7,8,12] Perovskites have also been shown to have self-healing capabilities when compressive stress is applied at room temperature or with heat treatments.[14] This self-healing behavior is a result of mechanical deformation and mass transport along the surfaces of cracks within the perovskite film,[14] which is analogous to the diffusion bonding process that occurs during lamination. Past studies have also shown an increase in grain domain size after lamination, which can be beneficial to PSC performance and stability.[7,8] Therefore, there is a need to deepen our knowledge of the mechanisms that guide the lamination process, which could enable rational control of the resulting microstructure and functional properties of the perovskite material.

In this study, we systematically investigate the role of lamination parameters (temperature, time, and pressure) during diffusion bonding at the HP-HP interface. The percentage of area that is successfully bonded during lamination is quantified using mechanical separation and post-mortem optical analysis. The steady-state photoluminescence (PL) intensity of the films is also measured after lamination to understand changes in the optoelectronic properties of the film, which are relevant to solar cell performance.[15−18] Additionally, the trends in apparent grain domain size were measured using scanning electron microscopy. Using a design of experiments to sample the parameter space, the observed trends in the material properties and the uncertainty surrounding these trends were quantitatively analyzed by performing a Gaussian process regression.

Among the process parameters studied, temperature was found to be the most important lamination parameter to control the measured properties. A high bonding temperature of 150 °C increases the bonded area up to 95% and results in significant increases in apparent grain domain size and PL intensity. In contrast, lamination pressure and time had less significant effects over the parameter ranges tested, suggesting an opportunity to increase throughput and decrease the applied force in a manufacturing setting. Finally, L-PSC devices were fabricated, and an increase in the short-circuit current (J_{SC}) at elevated lamination temperatures was found to be the

https://doi.org/10.1021/acsami.4c12379
ACS Appl. Mater. Interfaces 2024, 16, 58657−58667

primary factor that caused an improvement in the power conversion efficiency. These results illustrate the importance of achieving a large percentage of area bonded to maximize carrier collection efficiency and reduce recombination at the bonded interface. By deepening our understanding of these process-structure-property relationships, in the future, manufacturers can optimize their lamination process based on a specific objective function, such as maximizing throughput and/or minimizing cost and energy input requirements.

EXPERIMENTAL METHODS

Perovskite Deposition. The composition of the HP solutions used in this study is $FA_{0.8}MA_{0.15}Cs_{0.05}PbI_{2.6}Br_{0.4}$ (~250 nm thick before lamination) with 3 wt % excess PbI_2, corresponding to a bandgap of ~1.6 eV. The HP precursor solution was prepared by adding the following substances to a glass vial in the order listed and stirring in an argon-filled glovebox for at least 15 min: 18 mg of (CsI; Fischer Scientific), 204.6 mg of (FAI; Greatcell Solar), 23 mg of methylammonium bromide (MABr; Greatcell Solar), 77 mg of lead bromide ($PbBr_2$; Alfa Aesar), 606.7 mg of lead iodide (PbI_2; Fischer Scientific), 1.6 mL of dimethylformamide (DMF; Acros Organics, USA), 0.4 mL of dimethyl sulfoxide (DMSO; Sigma-Aldrich, USA). The solution was used within four hours of mixing.

Precleaned substrates (25 × 25 × 0.14 mm) were spin-coated by drop casting ~200 μL of HP precursor solution and then rotating at 6000 rpm. After 20 s of spinning (60 s before the end of the program), ~200 μL of chlorobenzene (Sigma-Aldrich, USA) was dispensed onto the substrates in a steady stream and rotated for 60 more seconds at 6000 rpm. Afterward, the HP-coated substrates were annealed on a hot plate for 50 min at 100 °C. Further details on the spin-coating experimental methods are provided in Supporting Information section SI 1 A,B.

Lamination Process. All of the HP-coated substrates were laminated using a hydraulic hot press with a custom-designed jig.[5] The jig and hot press were heated to the desired lamination temperature and given at least 10 min to reach steady-state. Two HP-coated substrates were loaded into the jig face-to-face such that the HP thin films contacted each other. The jig was loaded into the hot press and pressure was applied, allowing for diffusion bonding to occur at the HP-HP interface between the glass substrates (additional details in SI 1 C). Finally, the jig was unloaded and cooled down for ~4 min before the samples were extracted for characterization.

Materials Characterization. Steady-state PL spectra were collected using a class II 520 nm laser and a compact spectrometer (CCS200, Thorlabs). PL was measured 3 times toward the center of the sample (additional details in SI 1 E). For post-mortem optical analysis, the samples were delaminated by inserting a razor blade as a wedge between the glass substrates.[19] Optical imaging was performed using a digital microscope (VHX 7100, Keyence Corp). The bonded area was calculated from the post-mortem optical microscope images using a custom MATLAB software (additional details in SI 1 D). The apparent grain domain size of the post-mortem HP films was measured using a high-resolution scanning electron microscope (SEM) (Tescan Mira3, USA). The apparent grain domain size was calculated from these images using the linear intercept method[20] with a multiplying factor of 1.6 (further details in SI 1 F).

Statistical Framework for Analysis. A design of experiments (DOE) was employed to explore the processing parameter space of temperature, time, and pressure. A Box−Behnken design was used for the initial space-filling DOE in this study.[21] Informed by these initial experiments, additional data points were sampled to further resolve the observed trends (Figure 1).

A Gaussian process regression (GPR) was performed to describe the trends of how the materials characterization data depend on the lamination parameters. The GPR analysis provides a fit to the experimental data across the measured parameter space in an interpretable and statistically rigorous way. GPR is a machine-learning modeling method based on Bayesian probability theory that is used

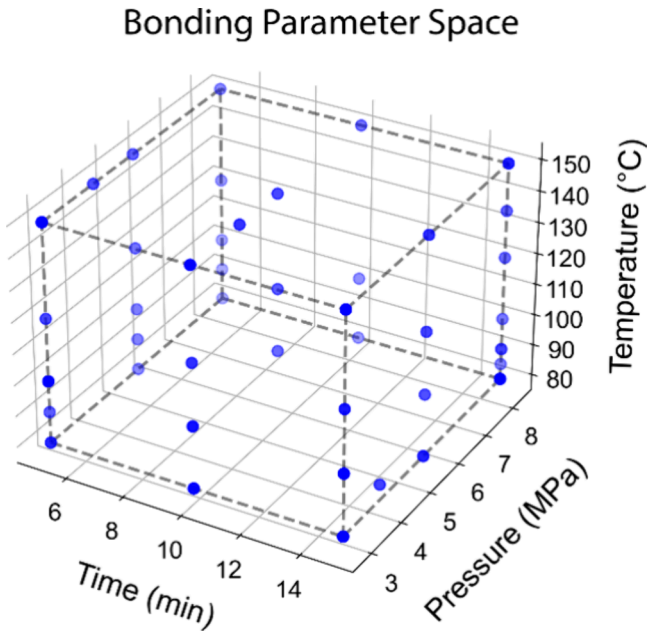

Figure 1. Bonding parameter space explored in this study, with the experimentally sampled lamination conditions marked in blue.

for this task because of its ability to capture general modeling relationships, its built-in uncertainty quantification, and its robustness to noisy and sparse data sets.[22,23] In this study, the GPR analysis was used to produce response surface plots that allow for a visualization of the trends in the parameter space.[24,25] Further details on the methods used for the GPR analysis are provided in the Supporting Information (SI 2).

Device Fabrication. Prepatterned fluorine-doped tin oxide (FTO) coated glass and Au/Ni-coated glass substrates were precleaned following the same procedures as the glass substrates (SI 1 A). A compact layer of SnO_x was deposited as the ETL on Au/Ni-coated glass substrates by spin-coating a 4% (v/v) diluted SnO_x colloidal solution (Alfa Aesar, USA) in DI water at 3000 rpm for 30 s. This process was performed in two passes, with each pass followed by a baking step at 150 °C for 30 min.

A bilayer of NiO_x/MeO-2PACz was deposited on top of the patterned FTO substrates as the HTL. First, NiO_x was spin-coated using the procedure described in Yadavalli et al., which includes an annealing step at 400 °C for 1 h.[5] A MeO-2PACz SAM was deposited on top of the freshly prepared NiO_x layer by first dissolving 0.3 mg/mL MeO-2PACz powder in ethanol and then spin-coating at 3000 rpm for 45 s, followed by annealing on a hot plate at 100 °C for 10 min. Next, perovskite layers were spin-coated on each of the two transport layer half stacks, which were subsequently laminated using the methods described above. For the devices, a 2× higher concentration of HP precursor with the same solvent weight ratio was used compared to the HP films that were directly deposited on glass substrates. The as-deposited films deposited with a 2× concentration were ~450 nm thick (SI 1 G), and after lamination, the HP layer thickness in the device stack was ~900 nm (Figure S3). This is consistent with previous studies that have shown that HP layer thicknesses of ~1 μm are optimal for PSCs.[26−28]

Device Characterization. The $J-V$ characteristics of the L-PSCs were measured using a Gamry Interface 5000 potentiostat under simulated 1-sun illumination (AM1.5G, 100 mW·cm^{-2}) produced by a Class ABA solar simulator (Abet Technologies, USA) in ambient conditions (room temperature, 40−60% relative humidity). The light intensity was calibrated with a standard silicon reference cell (Abet Technologies, model 15151). Measurements were performed in reverse-scan mode (from V_{OC} to J_{SC}) followed by forward-scan mode (from J_{SC} to V_{OC}). The active area of each device was measured under a digital optical microscope (VHX 7100, Keyence Corp). All of the L-

https://doi.org/10.1021/acsami.4c12379
ACS Appl. Mater. Interfaces 2024, 16, 58657−58667

Scheme 2. Illustration of a Diffusion Bonding Process, Showing (A) the Initial Separate Films, (B) Normal Stress and Diffusion Flux during Bonding, and (C) Resulting Bond Formation, Grain Growth, and Remaining Small Voids after Bonding

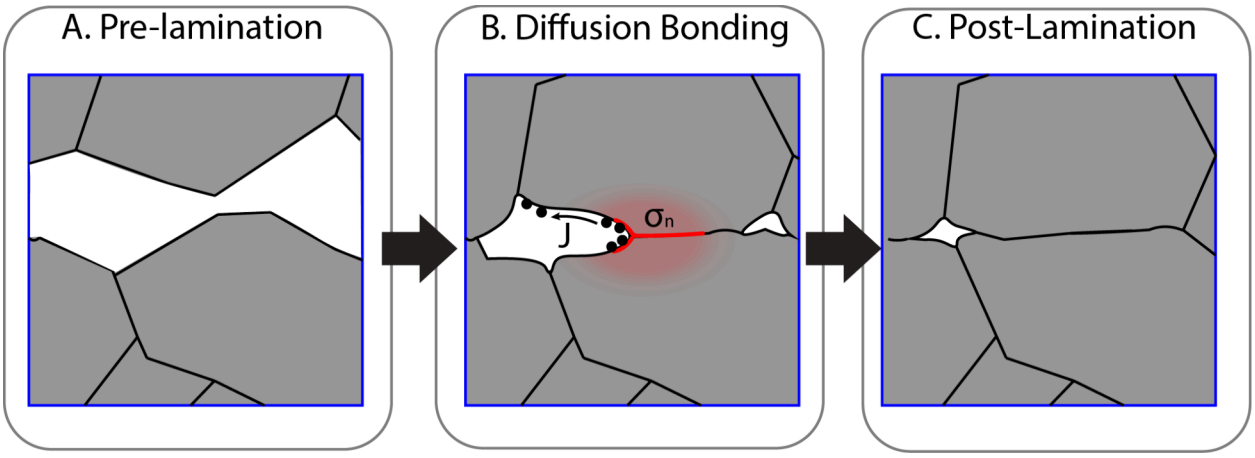

PSCs were aged in a glovebox for about a week before measurements were conducted without any preconditioning.

RESULTS AND DISCUSSION

A. Diffusion Bonding Fundamentals. Diffusion bonding is a common manufacturing technique used to join two materials by pressing them together, typically under elevated temperatures.[29] This can be performed with similar or dissimilar materials; here we focus on the diffusion bonding at a nominally identical HP-HP interface, which we have previously shown enables L-PSC devices with power conversion efficiencies (PCE) of 21%.[5]

Diffusion bonding is influenced by the properties of the material being bonded (e.g., surface roughness, elastic modulus, yield strength, diffusion coefficient), the surrounding environment in which bonding takes place, and the process parameters of pressure, temperature, and time.[29] By tuning these processing parameters, the resulting microstructure and defects that are present can be altered. By controlling the process-structure relationships during lamination, the resulting mechanical and functional properties of the bonded materials can be modulated, including bond strength/toughness, optoelectronic properties, and other application-specific properties of interest. A detailed understanding of these process−structure−property relationships is thus important when designing a material system with targeted performance metrics. Here, we provide a brief overview of the fundamentals of the diffusion process, to provide context for the following results and discussion.

During diffusion bonding, elastic and plastic deformation of the material surfaces can occur as a result of the applied pressure, creating intimate contact between the two surfaces. This mechanical deformation is coupled with diffusion of atomic or molecular species along and across the bonding interface (Scheme 2B). As a result of these coupled deformation and diffusion processes, chemical bonds can form along the interface (Scheme 2C).[29]

The initial surfaces will have a defined roughness and contact will occur at local asperities, with the actual contact area, A_c, being much less than the nominal contact area, A. As argued by Bowden and Tabor,[30] there will be a relationship between the nominal pressure, P, (defined as $P = N/A$, where N is the applied normal force) and the actual contact area, given by

$$P = H_c A_c \tag{1}$$

where H_C is the hardness, which is approximately equal to three times the yield strength. Accordingly, the contact area increases with either increasing pressure or decreasing hardness.

After initial contact has been established across the surface asperities, growth can occur by diffusion along the interface to fill the voids.[31−33] Interfacial diffusion is driven by a gradient in the chemical potential, μ_c, associated with the normal stress (σ_n, defined as positive for tension and negative for compression) across the interface:[34]

$$\mu_c = -\Omega\sigma_n \tag{2}$$

where Ω is the atomic volume. The diffusional flux, J, is proportional to the diffusion coefficient, D, and the derivative of the normal stress along the contact area (eq 2 and Scheme 2), so that

$$J = D\Omega \frac{d\sigma_n}{dx} \tag{3}$$

where x is position. The functional form of the normal stress is established as a result of the interaction between the applied pressure, and the need to maintain continuity of chemical potential with the curved surface at the tip of the void. The diffusion coefficient is exponentially related to the temperature, T,

$$D = D_0\, e^{-E_A/(k_B T)} \tag{4}$$

where D_0 is the self-diffusion coefficient, E_a the activation energy, and k_B is Boltzmann's constant. Therefore, temperature is an important parameter in the bonding process.

If diffusion kinetics are rate limiting, one would expect the bonded region to grow as the diffusion length (L_D) grows with time, t,

$$L_D = \sqrt{Dt} \tag{5}$$

The formation of a bonded interface also relies on a chemical reaction to form the bond across what will generally be misoriented grains at the interface. In general, it is possible that this step could be rate limiting.

Together, these equations provide a physical framework for rationalizing the trends observed with respect to the lamination parameters that are varied in this study. While a full

https://doi.org/10.1021/acsami.4c12379
ACS Appl. Mater. Interfaces 2024, 16, 58657−58667

multiphysics simulation of the diffusion bonding process would involve a more complex analysis that is beyond the scope of this study, the linear and nonlinear dependences of the mechanical, thermal, and chemical processes occurring will control the resulting material properties, which will be experimentally measured and analyzed in the following sections.

B. Percent Bonded Area. We define percent bonded area (PBA) as the percentage of the interfacial area that was successfully bonded during lamination. To quantify the PBA of the samples after lamination, the two glass substrates were separated by inserting a razorblade as a wedge (Figure 2A). After this separation process, the exposed surfaces of the two substrates were imaged using optical microscopy to analyze the remaining film geometry on each side.

We identified three distinct types of regions on each substrate. In regions where no perovskite layer was visible, the transparent glass substrate was exposed. These exposed regions correspond to locations where the bonded perovskite layers were transferred to the opposite substrate during the separation process. This can be observed in Figure 2B and C, where the exposed regions on one side are the mirror image of what we refer to as "transferred regions" on the other side. These transferred regions are where the thickness of the perovskite layer after separation is double that of the original perovskite layers before diffusion bonding. Therefore, these regions are defined as the locations where the diffusion bonding was sufficiently strong that the two HP layers did not easily debond during the separation process. In other words, in these locations, the failure occurred at a perovskite-glass interface, rather than at the perovskite-perovskite lamination interface.

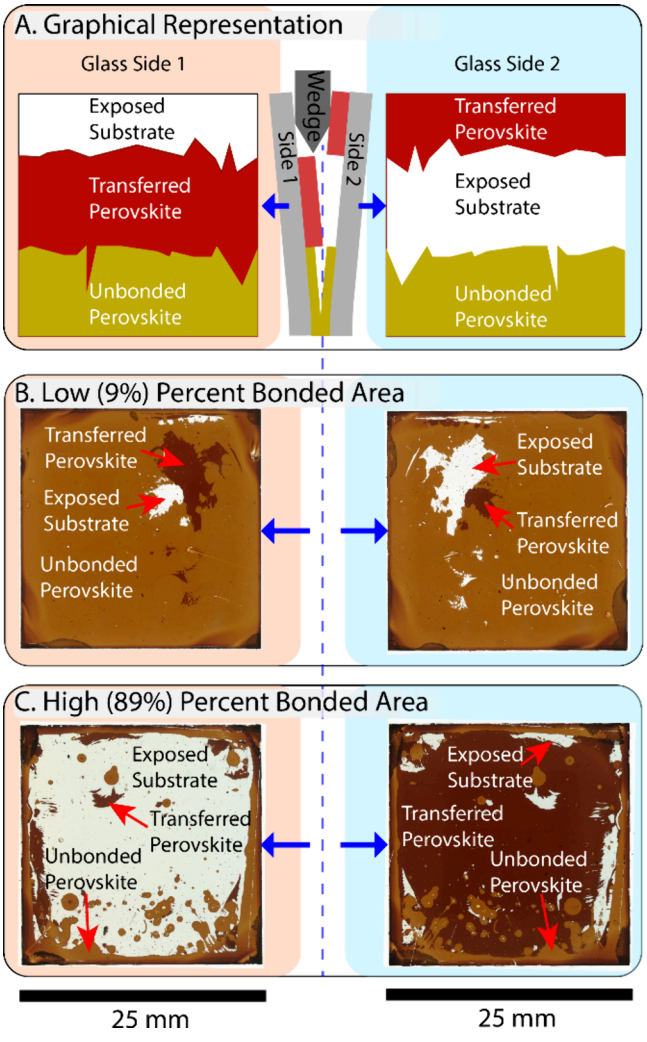

Figure 2. (A) Schematic illustration of the glass separation process, where the debonded substrates contain regions with exposed substrate, transferred perovskite, and unbonded perovskite layers. (B) Example of debonded substrates with a low PBA, showing largely unbonded perovskite regions on both substrates. (C) Example of debonded substrates with a high PBA, where the left substrate is mostly comprised of exposed glass and the right substrate is mostly covered by transferred perovskite.

The third category corresponds to regions where perovskite films were observed on both sides after separation. As shown in Figure 2B and C, these regions have a lighter optical contrast in comparison to the transferred regions. This indicates that a thinner film is present in the lighter regions, which results in the increased translucency of the samples during post-mortem optical microscopy. These lighter areas are labeled as unbonded regions, where separation occurred at the perovskite-perovskite interface. Although weak bonding may have been present in these regions after lamination, delamination occurred preferentially at the perovskite-perovskite interface as opposed to the perovskite-glass interface.

After the separation process, the PBA is calculated using quantitative image analysis (further details in SI 1 D and Figure S1). PBA is defined as the fractional area associated with the sum of the transferred and exposed regions, which are mirrored on each side. The measured PBA values ranged from 0 to 95% across the lamination parameter space studied. The results of the PBA analysis are shown in a series of response surfaces in Figure 3. As described in the Experimental Methods, these response surface plots were generated by performing a Gaussian process regression on the experimental data. A full list of the lamination conditions and PBA data are provided in Table S1.

Each of the response surfaces shown in Figure 3 presents the PBA trends as a function of temperature and pressure for a specific (fixed) lamination time. In other words, each subplot of Figure 3 represents a plane within the 3D parameter space cube (Figure 1), where the time for each plot is held constant. Figure 3A shows plots of the predicted mean values of PBA across the parameter space, and Figure 3B plots the standard deviation predicted by the GPR analysis at these conditions. In regions of the plot at or near the data points that were experimentally tested, the predicted standard deviation of the model closely matches the experimentally measured standard deviation, because the model has a lower degree of uncertainty at these conditions. Regions of high standard deviation indicate that the model has a higher degree of uncertainty in its predicted values at these conditions.

As shown in Figure 3A, there is a monotonic increase in PBA with increasing temperature across the entire lamination parameter space tested. Furthermore, increasing lamination pressure at a constant temperature (moving from left to right across an individual response surface in Figure 3A) also generally results in a higher PBA. Overall, this results in a general "up and to the right" trend, where the highest values of PBA are at elevated temperatures and pressures, which is expected based on the physics of diffusion bonding described in section A above. However, we observe that while higher

https://doi.org/10.1021/acsami.4c12379
ACS Appl. Mater. Interfaces 2024, 16, 58657−58667

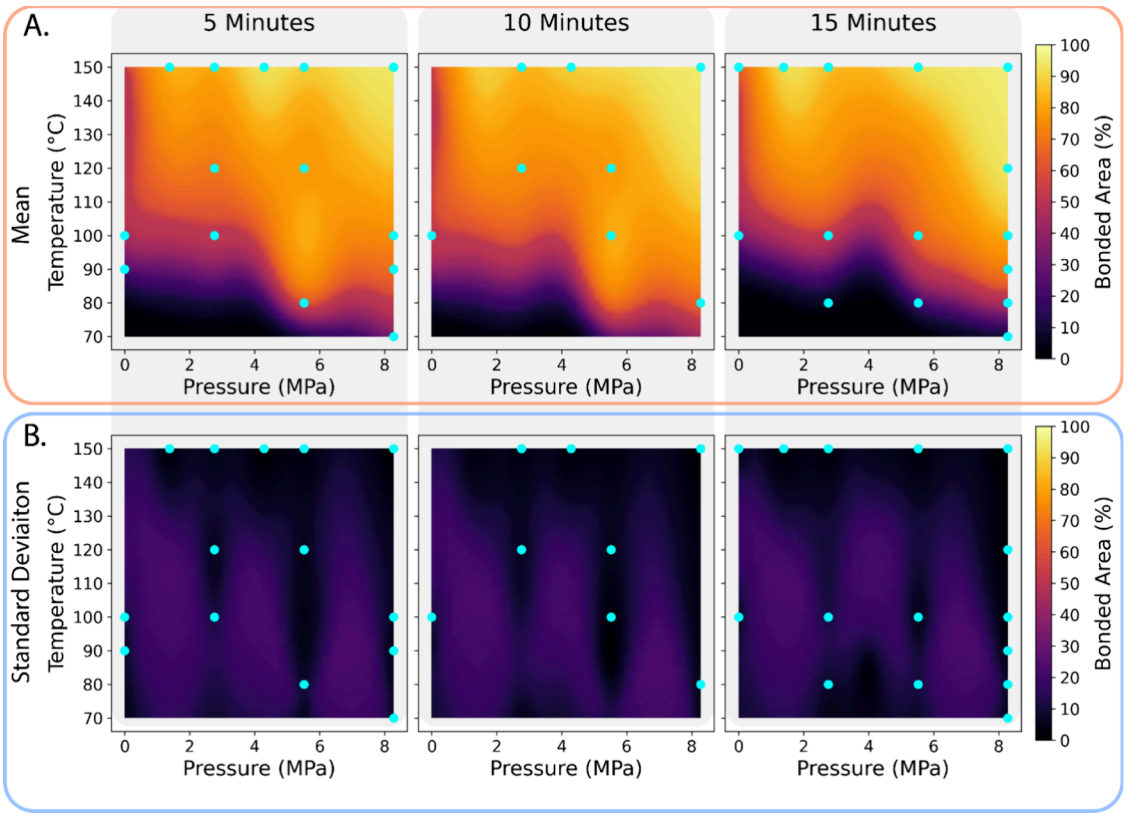

Figure 3. Response surfaces using the GPR analysis to show trends in (A) predicted mean and (B) predicted standard deviation in percent bonded area over the parameter space. Conditions in the parameter space where experimental data were collected are labeled by the cyan points.

temperatures (e.g., 150 °C) are sufficient to achieve a large PBA even at relatively low pressures (2 MPa), even at the highest pressure tested (8 MPa), PBA monotonically increases with increasing temperature. This illustrates that increasing pressure is more helpful at lower temperatures, but is not as critical at elevated temperatures, where faster diffusion occurs.

To further quantify the importance of each of the lamination process parameters on PBA, an analysis of variance (ANOVA) was performed. Across the data set, temperature was found to have by far the most significant influence on PBA with a P-value of 5×10^{-28}, compared to that of pressure (2×10^{-6}) and time (0.02) (Table S2). Furthermore, the relative importance of pressure diminishes at elevated temperatures, and is more significant at lower lamination temperatures of 80−100 °C, where increasing the pressure to 8 MPa results in an increases the PBA to values of ∼80%. This illustrates the interplay between these process parameters in a manufacturing context, where at a lower lamination temperature, higher pressures would be beneficial, but if temperature can be safely increased to 150 °C without damaging the perovskite or surrounding materials, a lower pressure can be used.

As described in section A, the lamination pressure, temperature, and time will have different influences on the physics of the diffusion-bonding process. The strong influence that temperature has on PBA can be traced back to the exponential dependence of the diffusion coefficient on temperature (eq 4). During the diffusion bonding process, surface and interfacial diffusion occur to fill-in void space and form chemical bonds.[29,35] While increasing time and pressure can also contribute to a higher PBA (particularly at lower temperatures), their influences are not expected to be exponential in nature. It is possible that an increase in temperature also leads to a sufficient reduction in hardness for large-scale contacts to be formed very rapidly, which allows for bonding across the interface.

The major influence of pressure is related to the initial contact mechanics, which defines the initial contact area between the two films (eq 1). Higher pressures will increase the gradient in the chemical potential, which is the driving force for diffusion (eq 2).[31] The influence of time comes primarily through the diffusion length, which increases with the square-root of the diffusion coefficient and time (eq 5).

The fact that temperature was observed to be the most important parameter in the bonding process, and there is essentially no effect of time after 5 min, suggests that either diffusion is very rapid, or it is the initial stage of the bonding process that is most important. This further suggests that there may be opportunities to increase the throughput of the lamination process in an industrial manufacturing setting.

C. Photoluminescence. To study the influence of the lamination processing parameters on the optoelectronic quality of the HP material after bonding, PL analysis was performed. PL is the measurement of emissive photon flux due to radiative recombination from a photoexcited semiconductor. It is a low-cost, high-throughput, and nondestructive method for evaluating solar cell materials and devices.[15] PL can be used to predict PSC performance based on the optoelectronic properties of the HP material within the solar cell. For example, the steady-state PL quantum yield relates directly to the quasi-Fermi level splitting in a PSC, which in turn provides the largest possible photovoltage extractable from an absorber.[15,36] Previous work has also shown that the PL intensity correlates with grain size of HP materials, with larger grains typically yielding a reduction in nonradiative recombi-

https://doi.org/10.1021/acsami.4c12379
ACS Appl. Mater. Interfaces 2024, 16, 58657−58667

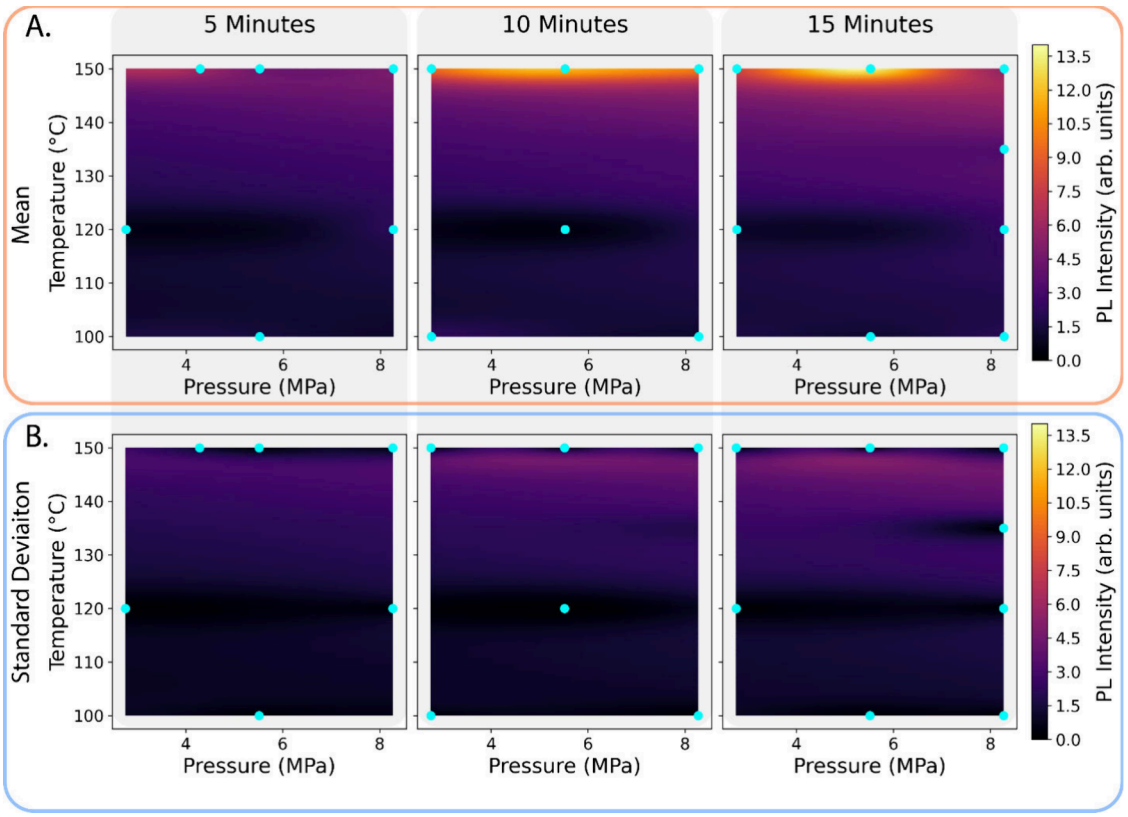

Figure 4. Response surfaces using GPR analysis to show tends in (A) predicted mean and (B) predicted standard deviation of PL peak intensity over the parameter space. Conditions in the parameter space where experimental data were collected are labeled by the cyan colored points.

nation, improved stability, and better PCE.[14,37,38] Therefore, PL can be used as a metrology tool to rapidly detect defects and heterogeneities in HP materials, saving cost and time for high-volume manufacturing processes. In this study, PL is used as a proxy for rapidly screening the HP semiconductor optoelectronic quality, as it allows for high-throughput quantification without the cost and time requirements of full device fabrication.

Based on the results from the PBA analysis, a new DOE was created for the PL measurements with a narrower temperature range from 100 to 150 °C. This range was chosen because the measured PBA values were relatively low at temperatures below 100 °C, and therefore are less likely to be relevant for device manufacturing. This illustrates the "funneling" approach of the experimental exploration in this study, where the widest range of process parameters was studied for PBA analysis, which was down-selected for PL analysis, and was then further down-selected for full device testing.

A GPR analysis of the mean and standard deviation of PL intensity is plotted in the response surfaces shown in Figure 4. The raw experimental PL data are shown in Table S3. The PL intensity was observed to increase substantially as the temperature was increased to 150 °C (Figure S2), which is consistent with the observed increase in average PBA with increasing temperature. However, while PBA increased more gradually with increasing temperature, a sharp, nonlinear increase in PL intensity was observed from 120 to 150 °C.

The trends in Figure 4 were further analyzed using ANOVA. Similar to the PBA experiments, temperature was by far the most significant parameter, with a P-value of 1×10^{-29}, compared to time (0.001) and pressure (0.03) (Table S4).

The differences between the response surfaces in Figures 3 and 4 suggest that although temperature is the most important lamination parameter for both PBA and PL, the underlying physical mechanisms that dictate the relative temperature dependencies of PBA and PL may be different. A potential explanation for the sharp increase in PL at elevated temperatures is a change in grain size in the HP material during lamination. The apparent grain domain size was measured from post-mortem SEM images of the laminated HP materials at 100, 120, and 150 °C (Figure 5). Similar to the observed trends in PL intensity, the extent of apparent grain domain growth during lamination is highly sensitive to temperature. In particular, while some grain growth occurs between 100 and 120 °C, a more significant increase in apparent grain domain size was observed when the temperature was increased from 120 to 150 °C. This grain-growth behavior was further validated by performing cross-sectional SEM analysis of devices laminated at 120 and 150 °C (Figure S3).

The observation of grain growth during lamination at elevated temperatures is consistent with a previous study that also observed grain growth in HP materials under applied pressure and temperatures,[8] and is supported by the theory of grain coarsening.[39,40] In addition, small quantities of PbI_2 have been shown to form during lamination at 150 °C,[5] which can have passivating effects when present in low quantities.[41] In the future, physics-based modeling of the microstructure evolution during lamination will be valuable to provide deeper insights into these relationships.

Overall, the fact that both the PL intensity and apparent grain domain size experience a sharp increase as temperature is increased from 120 to 150 °C, provides evidence to suggest

https://doi.org/10.1021/acsami.4c12379
ACS Appl. Mater. Interfaces 2024, 16, 58657−58667

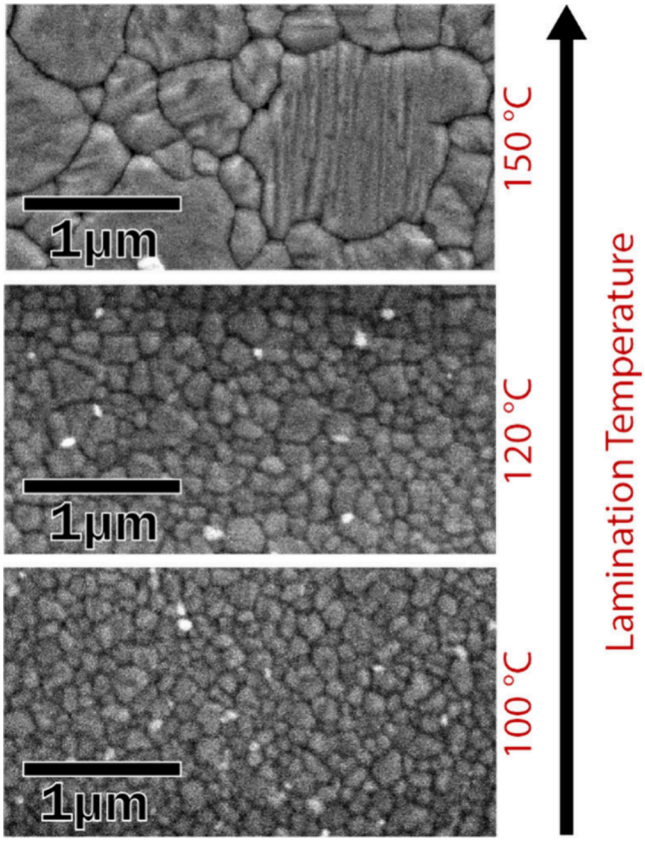

Figure 5. SEM images collected after diffusion bonding, showing the change in apparent grain domain size as a function of lamination temperature. Samples were bonded at 15 min, 8 MPa, and the temperatures are indicated in the subpanels.

that the origins of the PL trends are correlated with the HP microstructure. These results demonstrate the importance of understanding the coupled process-structure-property relationships during lamination, which can be used for future tuning of the process to rationally control the resulting structural and functional properties of the HP material.

D. Impact of Lamination Temperature on Device Performance. As described in the previous sections, both the PBA and PL analyses showed that temperature is the parameter that has the strongest influence on the lamination process. This illustrates the power of using high-throughput and low-cost screening methods to identify the critical process-structure relationships, which would have been more slow and costly to perform if a complete PSC device architecture were to be fabricated for each condition. Equipped with this knowledge, we down-selected a small subset of conditions to test with full L-PSC devices, where we examined the effects of lamination temperature as the key parameter. In these experiments, pressure and time were held constant at 8 MPa and 15 min, respectively.

The L-PSC material system and architecture were selected based on our previous study, which demonstrated high power-conversion efficiencies and good device stability.[5] L-PSC devices were fabricated using SnO_X as the ETL and a bilayer of NiO_X and MeO-2PACz as the HTL, which are contacted using gold and FTO electrodes, respectively. Further details on the fabrication procedure are included in the Experimental Methods. This combination of transport layers was chosen because they result in low PL quantum yield losses.[42]

We further note that this combination of solution processing (including SAM passivation) and postdeposition annealing of both transport layers is uniquely enabled by the processing flexibility offered by the lamination process. In contrast, the conventional sequential deposition process restricts the material and processing options of the transport, passivation, and contact layers that are deposited on top of the chemically and thermally sensitive HP layer. The SnO_X cannot be processed using aqueous solutions on top of the HP, as water

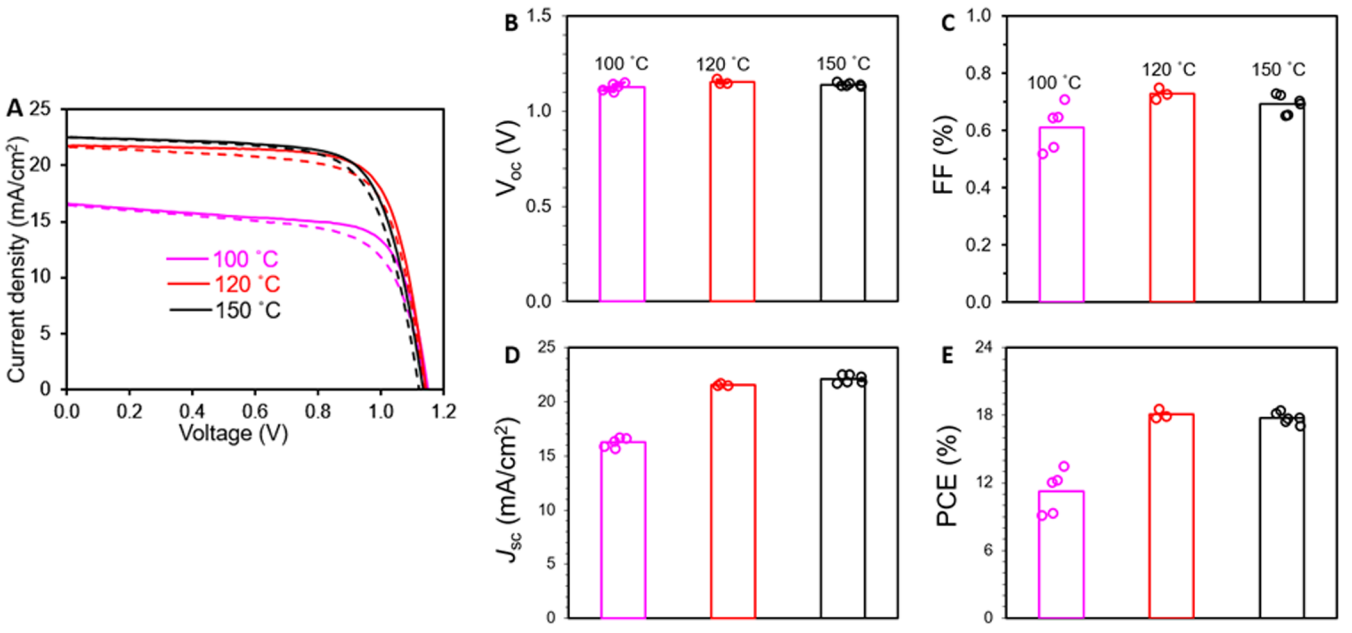

Figure 6. Device performance statistics as a function of lamination temperature. (A) $J-V$ characteristics in reverse (solid) and forward (dashed) scans for devices using SnO_X ETL and a bilayer of NiOx and MeO-2PACz SAMs HTL (B) V_{OC}, (C) fill factor, (D) J_{SC}, and (E) PCE. The data are from $N = 5$ repeat trials for 100 °C, $N = 3$ for 120 °C, and $N = 5$ for 150 °C.

https://doi.org/10.1021/acsami.4c12379
ACS Appl. Mater. Interfaces 2024, 16, 58657−58667

degrades the perovskite film. Similarly, MeO-2PACz SAM cannot be formed on top of the perovskite layer because it does not provide an −OH terminated surface.

After processing the half-stacks in parallel, the final lamination step was performed at the HP-HP interface, as shown in Scheme 1. Lamination was performed at temperatures of 100, 120, and 150 °C. This was followed by device characterization, with the current−voltage (J−V) responses presented in Figure 6A and statistics of the critical performance metrics (PCE, V_{OC}, J_{SC}, and fill factor) shown in Figure 6B−E.

The highest performing device among the samples that were laminated at a lower temperature of 100 °C had a measured PCE of 13.5%, V_{OC} of 1.15 V, J_{SC} of 16.6 mA/cm^2, and FF of 0.707. The performance is mainly limited by a low short-circuit current. A low J_{SC} is expected to arise from incomplete bonding at the laminating interface at this temperature, as evidenced by the low PBA values. Owing to this incomplete bonding at low temperatures, a significant fraction of the interfacial area will have voids remaining. Regions that have a higher fraction of remaining (microscopic) voids will have a lower interfacial fracture toughness, and are thus more likely to debond at the HP-HP interface when the razorblade is inserted (Figure 2). The presence of these regions with a high void density within a L-PSC could also limit the transport of photogenerated carriers across the interface and effectively reduce the active area of the device. The exposed surface area in unbonded regions could also contribute to increased charge-carrier recombination, which would further reduce J_{SC} by lowering the quantum efficiency.

When the lamination temperature was increased to 120 °C, the champion PCE increased to 18.6%, with aV_{OC} of 1.14 V, a J_{SC} of 21.7 mA/cm^2, and a FF of 0.748. This improvement is primarily due to a sharp increase in J_{SC}. We attribute these improvements to the increase in PBA at 120 °C, which provides a more continuous pathway for the transport of carriers and a reduced rate of surface recombination in the unbonded regions, compared to the 100 °C condition.

When the lamination temperature was further increased to 150 °C, the champion device had a PCE of 18.4%, aV_{OC} of 1.13 V, a J_{SC} of 22.5 mA/cm2, and a FF of 0.721. When comparing the devices that were laminated at 120 and 150 °C, there was not a significant change in device performance. In particular, we note that the V_{OC} and FF at 150 °C do not demonstrate any statistically significant improvement when compared to 120 °C, despite the fact that the PL intensity and apparent grain domain size were both observed to increase from 120 to 150 °C. Furthermore, the fact that the J_{SC} increased significantly from 100 to 120 °C and then reached a plateau at 150 °C agrees well with the trends in PBA under these lamination conditions (Figure 3A and Figure S4). Collectively, these observations illustrate that within the range of lamination parameters tested, device performance is less limited by the optoelectronic quality of the HP material itself (because an increase in PL intensity and apparent grain domain size did not significantly improve device performance), and is instead more limited by the continuity of bonding along the laminated interface.

CONCLUSION

This study provides new insights into the interplay between the lamination parameters (pressure, temperature, and time), bonded area, HP microstructure, optoelectronic properties, and device performance. A combination of Design of Experiments and Gaussian process regression analysis are used to present the trends within the parameter space. The key findings of this study are summarized below.

1. Within the range of conditions explored, temperature was observed to have the most significant influence on both PBA and PL intensity, as supported by ANOVA analysis. The strong temperature dependences observed can be attributed to the exponential dependence of diffusion coefficient on temperature.

2. While both PBA and PL were observed to increase with temperature, PBA increases more continuously with increasing temperature, while PL exhibited a sharp, nonlinear increase at elevated temperatures. This suggests that the underlying physical processes governing PBA and PL may differ. In particular, PBA is likely controlled by surface and interfacial diffusion along the lamination interface. On the other hand, PL shows a direct correlation with the increase in apparent grain domain size.

3. By performing lamination at elevated temperatures, a high PBA and PL can be achieved over a wide range of pressure and time conditions. This suggests that when lamination is performed at elevated temperatures, there is an opportunity to increase process throughput and decrease the required mechanical force applied. On the other hand, if lamination is performed at lower temperatures, the application of additional pressure can have some benefits. Overall, the understanding of these coupled dependences can allow for improved process optimization in a manufacturing setting, where the objective function may be weighted based on throughput, energy, and/or cost requirements.

4. The trends observed in the PBA and PL data allowed for a down-selection of the processing parameters for full L-PSC devices, where we focused on temperature as the most important parameter. L-PSC devices were fabricated at lamination temperatures of 100, 120, and 150 °C. An increase in temperature from 100 to 120 °C significantly improved the PCE, and a plateau in device performance was observed when temperature was further increased to 150 °C. The largest improvements with increasing temperature were in the J_{SC}, which is associated with an increase in PBA. These results suggest that L-PSCs are more limited by PBA than grain size or PL intensity under these conditions.

This study deepens our knowledge of the relationships between process parameters, material structure, and functional properties during lamination of HP interfaces. These insights are essential to optimizing material performance and, in the future, will accelerate the translation of this technology toward scalable manufacturing techniques such as continuous sheet-to-sheet or roll-to-roll lamination. Furthermore, the statistical model developed in this study will provide a basis to inform physics-based modeling at multiple length scales, ranging from lamination machinery to material microstructure. Because lamination is a versatile approach that can enable new material combinations and device architectures, L-PSCs have the potential to create low-cost, mass-produced PSCs to improve the affordability and increase the deployment of solar energy.

https://doi.org/10.1021/acsami.4c12379
ACS Appl. Mater. Interfaces 2024, 16, 58657−58667

■ ASSOCIATED CONTENT

Supporting Information

The Supporting Information is available free of charge at https://pubs.acs.org/doi/10.1021/acsami.4c12379.

Further details on experimental methodology, percent bonded area analysis, photoluminescence procedures, apparent grain domain size analysis, the Gaussian process regression model, ANOVA statistics, and experimental data (PDF)

■ AUTHOR INFORMATION

Corresponding Author

Neil P. Dasgupta − *Department of Mechanical Engineering, University of Michigan, Ann Arbor, Michigan 48109, United States; Department of Materials Science & Engineering, University of Michigan, Ann Arbor, Michigan 48109, United States;* orcid.org/0000-0002-5180-4063; Email: ndasgupt@umich.edu

Authors

Clare L. Lanaghan − *Department of Mechanical Engineering, University of Michigan, Ann Arbor, Michigan 48109, United States*

Oluka Okia − *Department of Mechanical Engineering, University of Michigan, Ann Arbor, Michigan 48109, United States*

Thomas Coons − *Department of Mechanical Engineering, University of Michigan, Ann Arbor, Michigan 48109, United States*

Srinivas K. Yadavalli − *Department of Mechanical Engineering, University of Michigan, Ann Arbor, Michigan 48109, United States*

Jack R. Palmer − *Materials Science and Engineering Program, University of California, San Diego, La Jolla, California 92093, United States*

Mengyao Zhang − *Department of Mechanical Engineering, University of Michigan, Ann Arbor, Michigan 48109, United States*

Karrer Hersh − *Department of Mechanical Engineering, University of Michigan, Ann Arbor, Michigan 48109, United States*

Moses Kodur − *Department of Chemical and Nano Engineering, University of California, San Diego, La Jolla, California 92093, United States*

Orlando Trejo − *Department of Mechanical Engineering, University of Michigan, Ann Arbor, Michigan 48109, United States*

Sean P. Dunfield − *Materials Science and Engineering Program, University of California, San Diego, La Jolla, California 92093, United States*

M. D. Thouless − *Department of Mechanical Engineering, University of Michigan, Ann Arbor, Michigan 48109, United States; Department of Materials Science & Engineering, University of Michigan, Ann Arbor, Michigan 48109, United States*

David P. Fenning − *Materials Science and Engineering Program and Department of Chemical and Nano Engineering, University of California, San Diego, La Jolla, California 92093, United States;* orcid.org/0000-0002-4609-9312

Xun Huan − *Department of Mechanical Engineering, University of Michigan, Ann Arbor, Michigan 48109, United States*

Complete contact information is available at: https://pubs.acs.org/10.1021/acsami.4c12379

Author Contributions

†C.L.L. and O.O. contributed equally.

Notes

The authors declare no competing financial interest.

■ ACKNOWLEDGMENTS

This work was supported in part by the U.S. Department of Energy's Office of Energy Efficiency and Renewable Energy (EERE) under Solar Energy Technologies Office (SETO) Agreement Number EE-0009521. This material is based upon work supported by the National Science Foundation under Grant No. 2328010. C.L.L., O.O., and T.C. acknowledge support from the National Science Foundation Graduate Research Fellowship Program under Grant No. DGE-1256260. O.T. acknowledges the support of the Department of Energy (DOE) EERE Postdoctoral Research Award. Portions of this work were performed in Michigan Centre for Materials Characterization and Lurie Nanofabrication Facility, which are supported by the University of Michigan's College of Engineering.

■ REFERENCES

(1) Li, Z.; Klein, T. R.; Kim, D. H.; Yang, M.; Berry, J. J.; van Hest, M. F. A. M.; Zhu, K. Scalable Fabrication of Perovskite Solar Cells. *Nat. Rev. Mater.* **2018**, *3* (4), 18017.

(2) Park, N.-G.; Zhu, K. Scalable Fabrication and Coating Methods for Perovskite Solar Cells and Solar Modules. *Nat. Rev. Mater.* **2020**, *5* (5), 333−350.

(3) Shalan, A. E. Challenges and Approaches towards Upscaling the Assembly of Hybrid Perovskite Solar Cells. *Mater. Adv.* **2020**, *1* (3), 292−309.

(4) Ghaffari, A.; Saki, Z.; Taghavinia, N.; Byranvand, M. M.; Saliba, M. Lamination Methods for the Fabrication of Perovskite and Organic Photovoltaics. *Mater. Horiz.* **2022**, *9* (10), 2473−2495.

(5) Yadavalli, S. K.; Lanaghan, C. L.; Palmer, J.; Gayle, A. J.; Penley, D.; Okia, O.; Zaccherini, M.; Trejo, O.; Dunfield, S. P.; Fenning, D. P.; Dasgupta, N. P. Lamination of >21% Efficient Perovskite Solar Cells with Independent Process Control of Transport Layers and Interfaces. *ACS Appl. Mater. Interfaces* **2024**, *16* (13), 16040−16049.

(6) Jung, H.-Y.; Oh, E. S.; Kim, D. J.; Shim, H.; Lee, W.; Yoon, S.-G.; Lim, J.; Yun, J. S.; Kim, T.-S.; Yang, T.-Y. Adjusted Bulk and Interfacial Properties in Highly Stable Semitransparent Perovskite Solar Cells Fabricated by Thermocompression Bonding between Perovskite Layers. *ACS Appl. Mater. Interfaces* **2023**, *15* (26), 31344−31353.

(7) Dunfield, S. P.; Moore, D. T.; Klein, T. R.; Fabian, D. M.; Christians, J. A.; Dixon, A. G.; Dou, B.; Ardo, S.; Beard, M. C.; Shaheen, S. E.; Berry, J. J.; van Hest, M. F. A. M. Curtailing Perovskite Processing Limitations via Lamination at the Perovskite/Perovskite Interface. *ACS Energy Lett.* **2018**, *3* (5), 1192−1197.

(8) Dunlap-Shohl, W. A.; Li, T.; Mitzi, D. B. Interfacial Effects during Rapid Lamination within MAPbI3 Thin Films and Solar Cells. *ACS Appl. Energy Mater.* **2019**, *2* (7), 5083−5093.

(9) Schmager, R.; Roger, J.; Schwenzer, J. A.; Schackmar, F.; Abzieher, T.; Byranvand, M. M.; Nejand, B. A.; Worgull, M.; Richards, B. S.; Paetzold, U. W. Laminated Perovskite Photovoltaics: Enabling Novel Layer Combinations and Device Architectures. *Adv. Funct. Mater.* **2020**, *30* (9), 1907481.

(10) Gong, O. Y.; Seo, M. K.; Choi, J. H.; Kim, S.-Y.; Kim, D. H.; Cho, I. S.; Park, N.-G.; Han, G. S.; Jung, H. S. High-Performing Laminated Perovskite Solar Cells by Surface Engineering of Perovskite Films. *Appl. Surf. Sci.* **2022**, *591*, 153148.
(11) Li, J.; Xia, R.; Qi, W.; Zhou, X.; Cheng, J.; Chen, Y.; Hou, G.; Ding, Y.; Li, Y.; Zhao, Y.; Zhang, X. Encapsulation of Perovskite Solar Cells for Enhanced Stability: Structures, Materials and Characterization. *J. Power Sources* **2021**, *485*, 229313.
(12) Juarez-Perez, E. J.; Ono, L. K.; Qi, Y. Thermal Degradation of Formamidinium Based Lead Halide Perovskites into Sym-Triazine and Hydrogen Cyanide Observed by Coupled Thermogravimetry-Mass Spectrometry Analysis. *J. Mater. Chem. A* **2019**, *7* (28), 16912−16919.
(13) Wu, D.; Cui, Z.; Xue, T.; Zhang, R.; Su, M.; Hu, X.; Sun, G. Self-Encapsulated Wearable Perovskite Photovoltaics via Lamination Process and Its Biomedical Application. *iScience* **2023**, *26* (7), 107248.
(14) Yadavalli, S. K.; Dai, Z.; Zhou, H.; Zhou, Y.; Padture, N. P. Facile Healing of Cracks in Organic-Inorganic Halide Perovskite Thin Films. *Acta Mater.* **2020**, *187*, 112−121.
(15) Kirchartz, T.; Márquez, J. A.; Stolterfoht, M.; Unold, T. Photoluminescence-Based Characterization of Halide Perovskites for Photovoltaics. *Adv. Energy Mater.* **2020**, *10*, 1904134.
(16) Li, C.; Guerrero, A.; Huettner, S.; Bisquert, J. Unravelling the Role of Vacancies in Lead Halide Perovskite through Electrical Switching of Photoluminescence. *Nat. Commun.* **2018**, *9* (1), 5113.
(17) Braly, I. L.; deQuilettes, D. W.; Pazos-Outón, L. M.; Burke, S.; Ziffer, M. E.; Ginger, D. S.; Hillhouse, H. W. Hybrid Perovskite Films Approaching the Radiative Limit with over 90% Photoluminescence Quantum Efficiency. *Nat. Photonics* **2018**, *12* (6), 355−361.
(18) Kirchartz, T.; Krückemeier, L.; Unger, E. L. Research Update: Recombination and Open-Circuit Voltage in Lead-Halide Perovskites. *APL Mater.* **2018**, *6* (10), 100702.
(19) Chen, Y.; Ginga, N. J.; LePage, W. S.; Kazyak, E.; Gayle, A. J.; Wang, J.; Rodríguez, R. E.; Thouless, M. D.; Dasgupta, N. P. Enhanced Interfacial Toughness of Thermoplastic-Epoxy Interfaces Using ALD Surface Treatments. *ACS Appl. Mater. Interfaces* **2019**, *11* (46), 43573−43580.
(20) Mendelson, M. I. Average Grain Size in Polycrystalline Ceramics. *J. Am. Ceram. Soc.* **1969**, *52* (8), 443−446.
(21) Box, G. E. P.; Behnken, D. W. Some New Three Level Designs for the Study of Quantitative Variables. *Technometrics* **1960**, *2* (4), 455−475.
(22) Rasmussen, C. E.; Williams, C. K. I. *Gaussian Processes for Machine Learning*; The MIT Press, 2005.
(23) Schulz, E.; Speekenbrink, M.; Krause, A. A Tutorial on Gaussian Process Regression: Modelling, Exploring, and Exploiting Functions. *J. Math. Psychol.* **2018**, *85*, 1−16.
(24) Gardner, J. R.; Pleiss, G.; Bindel, D.; Weinberger, K. Q.; Wilson, A. G. GPyTorch: Blackbox Matrix-Matrix Gaussian Process Inference with GPU Acceleration. *arXiv* **2018**, 1809.11165.
(25) Wang, J. An Intuitive Tutorial to Gaussian Process Regression. *Comput. Sci. Eng.* **2023**, *25* (4), 4−11.
(26) Yang, Z.; Yu, Z.; Wei, H.; Xiao, X.; Ni, Z.; Chen, B.; Deng, Y.; Habisreutinger, S. N.; Chen, X.; Wang, K.; Zhao, J.; Rudd, P. N.; Berry, J. J.; Beard, M. C.; Huang, J. Enhancing Electron Diffusion Length in Narrow-Bandgap Perovskites for Efficient Monolithic Perovskite Tandem Solar Cells. *Nat. Commun.* **2019**, *10* (1), 4498.
(27) Li, K.; Zhang, S.; Ruan, Y.; Li, D.; Zhang, T.; Zhen, H. Optimization of Light Management Layers for Light Harvest of Perovskite Solar Cells. *Opt. Express* **2019**, *27* (16), A1004.
(28) Lin, R.; Xiao, K.; Qin, Z.; Han, Q.; Zhang, C.; Wei, M.; Saidaminov, M. I.; Gao, Y.; Xu, J.; Xiao, M.; Li, A.; Zhu, J.; Sargent, E. H.; Tan, H. Monolithic All-Perovskite Tandem Solar Cells with 24.8% Efficiency Exploiting Comproportionation to Suppress Sn(Ii) Oxidation in Precursor Ink. *Nat. Energy* **2019**, *4* (10), 864−873.
(29) Mechanisms of Bonding for Solid-State Welding Processes. In *Welding Fundamentals and Processes*; Lienert, T., Siewert, T., Babu, S., Acoff, V., Eds.; ASM International, 2011; pp 171−178, DOI: 10.31399/asm.hb.v06a.a0005574.
(30) Bowden, F. P.; Tabor, D. *The Friction and Lubrication of Solids*; Oxford Classic Texts in the Physical Sciences; Clarendon Press; Oxford University Press: Oxford, New York, 2001.
(31) Hull, D.; Rimmer, D. E. The Growth of Grain-Boundary Voids under Stress. *Philos. Mag.* **1959**, *4* (42), 673−687.
(32) German, R. M. 1 - Thermodynamics of Sintering. In *Sintering of Advanced Materials*; Fang, Z. Z., Ed.; Woodhead Publishing Series in Metals and Surface Engineering; Woodhead Publishing, 2010; pp 3−32. DOI: 10.1533/9781845699949.1.3.
(33) German, R. M. Chapter Seven - Thermodynamic and Kinetic Treatments. In *Sintering: From Empirical Observations to Scientific Principles*; German, R. M., Ed.; Butterworth-Heinemann: Boston, 2014; pp 183−226, DOI: 10.1016/B978-0-12-401682-8.00007-0.
(34) Herring, C. Diffusional Viscosity of a Polycrystalline Solid. *J. Appl. Phys.* **1950**, *21* (5), 437−445.
(35) Humphreys, J.; Rohrer, G. S.; Rollett, A. Chapter 11 - Grain Growth Following Recrystallization. In *Recrystallization and Related Annealing Phenomena (Third ed.)*; Humphreys, J., Rohrer, G. S., Rollett, A., Eds.; Elsevier: Oxford, U.K., 2017; pp 375−429, DOI: 10.1016/B978-0-08-098235-9.00011-2.
(36) Caprioglio, P.; Stolterfoht, M.; Wolff, C. M.; Unold, T.; Rech, B.; Albrecht, S.; Neher, D. On the Relation between the Open-Circuit Voltage and Quasi-Fermi Level Splitting in Efficient Perovskite Solar Cells. *Adv. Energy Mater.* **2019**, *9* (33), 1901631.
(37) Zhao, X.; Wang, Z.; Tian, W.; Yan, X.; Shi, Y.; Wang, Y.; Sun, Z.; Jin, S. A Positive Correlation between Local Photocurrent and Grain Size in a Perovskite Solar Cell. *J. Energy Chem.* **2022**, *72*, 8−13.
(38) Lin, X.; Chesman, A. S. R.; Raga, S. R.; Scully, A. D.; Jiang, L.; Tan, B.; Lu, J.; Cheng, Y. B.; Bach, U. Effect of Grain Cluster Size on Back-Contact Perovskite Solar Cells. *Adv. Funct. Mater.* **2018**, *28* (45), 1805098.
(39) Burke, J. E.; Turnbull, D. Recrystallization and Grain Growth. *Prog. Met. Phys.* **1952**, *3*, 220−292.
(40) Turnbull, D. Theory of Grain Boundary Migration Rates. *JOM* **1951**, *3* (8), 661−665.
(41) Jacobsson, T. J.; Correa-Baena, J.-P.; Halvani Anaraki, E.; Philippe, B.; Stranks, S. D.; Bouduban, M. E. F.; Tress, W.; Schenk, K.; Teuscher, J.; Moser, J.-E.; Rensmo, H.; Hagfeldt, A. Unreacted PbI2 as a Double-Edged Sword for Enhancing the Performance of Perovskite Solar Cells. *J. Am. Chem. Soc.* **2016**, *138* (32), 10331−10343.
(42) Warby, J.; Zu, F.; Zeiske, S.; Gutierrez-Partida, E.; Frohloff, L.; Kahmann, S.; Frohna, K.; Mosconi, E.; Radicchi, E.; Lang, F.; Shah, S.; Peña-Camargo, F.; Hempel, H.; Unold, T.; Koch, N.; Armin, A.; De Angelis, F.; Stranks, S. D.; Neher, D.; Stolterfoht, M. Understanding Performance Limiting Interfacial Recombination in Pin Perovskite Solar Cells. *Adv. Energy Mater.* **2022**, *12* (12), 2103567.